# PHOTONICS Research

# Spatially engineered nonlinearity in resonant metasurfaces

Anna Fedotova,[1,2,*] Mohammadreza Younesi,[2] Maximilian Weissflog,[2,3] Dennis Arslan,[1,2] Thomas Pertsch,[2,3,4] Isabelle Staude,[1,2,3] and Frank Setzpfandt[2,4]

[1]*Institute of Solid State Physics, Friedrich Schiller University Jena, 07743 Jena, Germany*
[2]*Institute of Applied Physics, Abbe Center of Photonics, Friedrich Schiller University Jena, 07745 Jena, Germany*
[3]*Max Planck School of Photonics, 07745 Jena, Germany*
[4]*Fraunhofer Institute for Applied Optics and Precision Engineering, 07745 Jena, Germany*
*Corresponding author: anna.fedotova@uni-jena.de*

**Spatial engineering of the nonlinear susceptibility $\chi^{(2)}$ in resonant metasurfaces offers a new degree of freedom in the design of the far-field response of second-harmonic generation (SHG). We demonstrate this by applying electric field poling to lithium niobate (LN) thin films, which inverts the spontaneous polarization and thus the sign of $\chi^{(2)}$. Metasurfaces fabricated in periodically poled LN films reveal the distinct influence of the $\chi^{(2)}$-patterning on the spatial distribution of the second harmonic. This work is a first step toward far-field engineering of SHG in metasurfaces with electric field poling.** © 2023 Chinese Laser Press

## 1. INTRODUCTION

During the past decade, several approaches to tailor second-harmonic generation (SHG) from metasurfaces—arrays of nano-resonators—were explored: geometries that sustain Mie- or Fano-resonances [1,2], different material systems [3,4], or active tuning with liquid crystals [5]. On the other hand, the second-order nonlinear susceptibility $\chi^{(2)}$ itself can be modified, for example, by vertically stacking different materials [6,7]. However, these approaches simultaneously modify the linear and nonlinear properties of the metasurfaces or require complex fabrication steps like molecular beam epitaxy. Alternatively, spatial engineering of the $\chi^{(2)}$-nonlinearity leaves the linear properties unchanged and thus decouples modification of the nonlinear properties. In addition, lithium niobate (LN) allows this decoupling to be achieved while relying solely on its own properties.

LN only recently made its way into nonlinear nanophotonics [1,8–11]. It is an excellent material for nonlinear processes: it is transparent from the ultraviolet to the mid-IR; it has a high second-order nonlinearity and a large electro-optic effect. Additionally, it possesses many other properties that are largely unexplored in nanophotonics, for example, ferroelectricity. Ferroelectric materials have a nonzero polarization even in the absence of an external electric field. Under normal conditions, this so-called spontaneous polarization is uniform in commercially available LN crystals, and they feature only one ferroelectric domain. When applying a strong electric field along the LN's optic axis, the crystalline $z$-axis (LN is an uniaxial

birefringent crystal), we can change certain ion positions inside the crystal. This will change the direction of the spontaneous polarization and form a ferroelectric domain with switched polarity. One of the consequences of the changed polarity is that in this domain the sign of the nonlinear susceptibility $\chi^{(2)}$ will be reversed. By applying an electric field to several regions of the crystal, we can thus create a spatial $\chi^{(2)}$-pattern [12]. The process of periodically inverting the ferroelectric domains in an LN crystal is called periodic poling. It is already widely used in integrated optics for quasi-phase-matching of the second harmonic (SH) [13–15]. Another interesting application of periodic poling is backward phase-matching [16] for second-harmonic pulse shaping [17], self-pulsing [18], or mirrorless optical parametric oscillators [19]. Together with different poling techniques [20–22], electric field poling has already been applied to create 2D or even 3D nonlinear photonic crystals [23–25] to control nonlinear frequency conversion, but so far has never been combined with resonant nanostructures. Recently, it became possible to reach submicron poling periods as small as 600 nm for $x$-cut [26–28] and 300 nm for $z$-cut [29,30] LN thin films, which makes electric field poling an interesting tool to control frequency conversion in nonlinear metasurfaces with subwavelength periodicity.

In this work, we experimentally demonstrate this approach by using a spatially inhomogeneous nonlinear susceptibility $\chi^{(2)}$ to engineer the SHG from resonant metasurfaces in lithium niobate. Our results add another degree of freedom in the design of nonlinear metasurfaces.

## 2. RESULTS

### A. Fabrication and Linear Characterization

Specifically, we apply periodic electric field poling to introduce a nonlinear diffraction grating due to the modulated $\chi^{(2)}$. Figure 1(a) shows an scanning electron micrograph (SEM) with the false colors of an example structure that we use experimentally for SHG. In the image, we identify two different types of structuring: a 2D array of resonant nanostructures with period $d$, which is etched into the LN thin film that was periodically poled before, and a 1D nonlinear grating with period $p$. The modulated $\chi^{(2)}$ is indicated by false blue/red colors and plus/minus signs. Both of these gratings will lead to diffraction of the second harmonic (SH) generated in the metasurface through nonlinear frequency conversion, where the ensuing diffraction orders in the reciprocal space of the wavevectors $\mathbf{k}_z$ and $\mathbf{k}_y$ are schematically shown in Fig. 1(b). The 2D geometric grating formed by the nanoresonators with period $d$, will lead to the orders marked by the blue dots. The $\chi^{(2)}$-grating with period $p$, where in the example $p = 2d$, will manifest itself as additional diffraction orders marked in green. In other words, this additional degree of freedom for nanophotonics, enabled by the nature of LN, allows us to manipulate the $k$-space of the SH generated by the resonant metasurface.

As a first step to realize a metasurface with periodic poling, we pole parts of a 600 nm thick $x$-cut LN thin film-on insulator (2 μm $SiO_2$) on an $x$-cut LN substrate (500 μm) with periods $p$ from 1 μm to 4 μm using electric field poling. The width of the poled regions in the $z$-direction is 20 μm, while the length along the $y$-direction is 200 μm. The poling process is performed mainly using the parameters developed in the previous work [28]. The electrode patterns (170 nm Cr covered by 30 nm Au) are fabricated on top of the LN thin film by a lift-off process. Next, we apply a high voltage (∼60 V/μm) signal to the electrodes. Depending on the poling period, we use different poling voltages to achieve the highest poling quality. For the parts where the domain growth is insufficient, we repeat the poling process several times. The poling quality is optically characterized by polarization-contrast microscopy. Afterward, the electrodes are removed.

The polarization-contrast microscopy image in Fig. 1(c) shows the resulting domain structure between two electrodes (black in the figure): the red false color marks the triangular regions where the sign of $\chi^{(2)}$ should be inverted while the blue color stands for the regions where $\chi^{(2)}$ should remain unchanged. Due to the stress on the border between these two ferroelectric domains, the polarization of transmitted light is slightly rotated, and we are able to image the actual domains with polarization-contrast microscopy. As inverted domains start growing from the positive to the negative electrode (from $+z$ side to $–z$ side), not all the width of the film is homogeneously poled, as can be seen in Fig. 1(c): the duty cycle (widths of the poled versus the nonpoled domains) varies from 50% next to the top electrode to ∼20% next to the bottom one.

After poling and removal of electrodes, the LN film is structured using electron-beam lithography and subsequent etching following the procedure described in Ref. [1]. To demonstrate the capabilities of our approach, we fabricate 1D metasurfaces (nanogratings) with various periods and 2D metasurfaces from arrays of nanoresonators in the shape of truncated nanopyramids with period $d$ of 1 μm. To later compare the effect of poling on SHG, we produce identical metasurfaces on the poled and on the nonpoled parts of the thin film. Below, we refer to them, respectively, as poled and nonpoled metasurfaces. Figure 1(a) shows an SEM image of one such poled 2D metasurface with an array of truncated nanopyramids with an ≈83° side wall angle.

To investigate the effect of poling on the linear properties of the resonant metasurfaces, we measure the linear transmittance
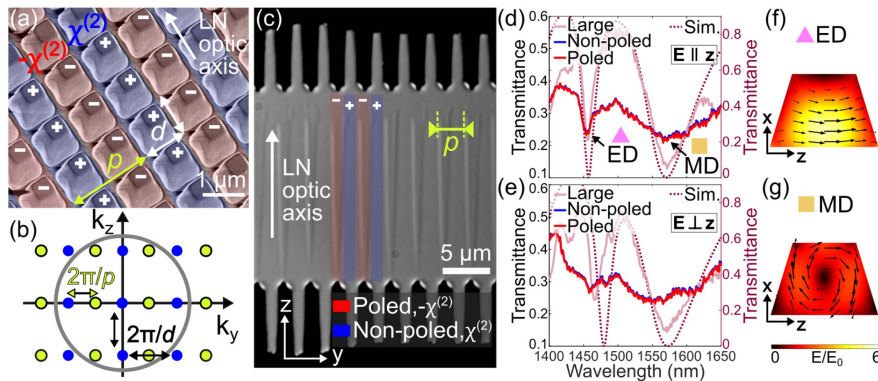


**Fig. 1.** (a) SEM image of an example metasurface. The false red color shows regions with altered by electric field poling second-order nonlinear susceptibility $\chi^{(2)}$. The false blue color marks the regions where $\chi^{(2)}$ was not affected. $d$ is the period of nanostructuring (or the geometric diffraction grating), and $p$ is the period of grating formed by alternating signs of $\chi^{(2)}$ (or the new nonlinear grating). (b) Scheme of the $k$-space (diffraction pattern) of such a metasurface as in (a) for SH. The blue orders appear from the nanostructure grating and the green ones from the additional nonlinear grating. In the experiment, we collected only the orders propagating under angles accepted by the NA of our collection objective (marked as a gray circle). (c) Polarization-contrast microscopy image of a poled LN thin film. Dark areas on the top and bottom are electrodes, and triangle areas in the middle are poled regions. False colors mark poled and nonpoled parts. The poling period here is $p = 3$ μm. (d) and (e) Experimental transmittance spectra of three metasurfaces with the same geometric parameters (left $y$-axis): poled metasurface (red), nonpoled metasurface (blue), and large nonpoled metasurface (pink) for polarization along the LN optic axis (d) and perpendicular to it (e). Dotted curves show simulated transmittance for an infinite metasurface (right $y$-axis). (f) and (g) Enhancement of the electric field inside a nanoresonator at two wavelengths: (f) electric dipole (ED) resonance, and (g) magnetic dipole (MD) resonance.

from poled (red curve) and nonpoled (blue curve) metasurfaces for polarizations along and perpendicular to the LN optic axis, as shown in Figs. 1(d) and 1(e), respectively. These metasurfaces have a relatively small area of 20 μm × 200 μm. Additionally, we measure the transmittance from a large, 200 μm × 200 μm, nonpoled metasurface with nominally the same geometric parameters [the solid pink line in Figs. 1(d) and 1(e)]. The dotted curves represent the simulated spectra calculated for an infinite periodic metasurface. For both polarizations, we notice that the spectra of poled and nonpoled metasurfaces are identical, which is expected, since the electric field poling does not affect the linear optical properties of LN. At the same time, the birefringence of LN leads to a different response for both polarizations, as evident from the spectra in Figs. 1(d) and 1(e). Furthermore, we can identify two Mie-type resonances: for the polarization along the LN optic axis, as shown in Fig. 1(d), the dip at ~1455 nm is dominated by the electric dipole (ED) mode (marked as ED with a triangle) and at ~1570 nm by the magnetic dipole (MD) mode (marked as MD with a square), similar to our previously fabricated metasurfaces [1]. From the simulations, it follows that the electric field at the ED resonance is enhanced 6-fold, whereas the enhancement is 3-fold at the MD resonance, as shown in Figs. 1(f) and 1(g). These resonances are Mie-type resonances strongly coupled to the lattice period of the metasurface [31].

Due to the small area, the metasurfaces with sizes 20 μm × 200 μm show noticeable but not very pronounced resonances. For comparison, the larger metasurface with nominally identical local geometry parameters shows a much better transmission modulation [31–33]. These spectra also correspond very well to the simulations done for an infinite array. Although we expect all the metasurfaces to have the same linear spectra, fabrication imperfections lead to slightly different metasurface geometries and therefore positions of resonances. For a smaller array size, even minor differences in the geometry of the nanoresonators play a large role and lead to

broadening of the metasurface's resonances and a decrease in the $Q$-factor [34,35].

### B. Second-Harmonic Generation

To measure second-harmonic generation, we use a nonlinear microscope (see the setup in Ref. [1]), where we excite the metasurfaces from the substrate side with linearly polarized femtosecond laser pulses (Mai Tai + OPO Inspire HF 100, Spectra-Physics, pulse duration 100 fs, repetition rate 80 MHz, spectral width at the FWHM 10 nm) at different telecom wavelengths with a peak intensity around 6 GW/cm². The resulting SH is imaged on a sensitive CCD camera (iXon3 EMCCD, Andor). In our setup, we can image the back focal plane of the collection objective (EC Epiplan 100x/0.85, Zeiss) and thus, the diffraction pattern of the SH emission. The pump beam waist had to be reduced to excite a smaller and therefore more homogeneously poled area to maximize the visibility of the $\chi^{(2)}$-diffraction orders. The resulting SH beam waist was around 6–8 μm at FWHM, corresponding to approximately 9 × 9 nanoresonators (estimated from the real-space SHG images in Fig. 2). Due to the domain inhomogeneity, the place of measurement on a poled metasurface influences the generated SH. For the final measurements, we select the metasurface's part that gave the strongest SHG signal into the $\chi^{(2)}$-orders. Most of the experiments are done with pump polarization along the LN optic axis to make use of the largest component of the LN second-order nonlinear coefficient $|d_{33}| = 19.5$ pm/V (value at 1313 nm [36]).

Figures 2(a)–2(h) show the SH signal in real space for different metasurfaces. Here and in further figures, the top row displays poled metasurfaces, where the $\chi^{(2)}$-distribution was modified [here, Figs. 4(a)–4(d)], and the bottom row displays nonpoled reference metasurfaces, where $\chi^{(2)}$ is the same everywhere [here, Figs. 4(e)–4(h)]. We also schematically show $\chi^{(2)}$-distributions in the top row. Each image is normalized to its maximum value. Although SH is being generated in
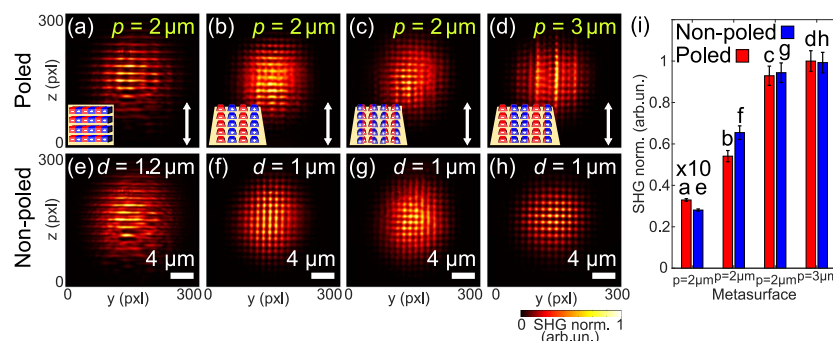


**Fig. 2.** (a)–(h) Experimental real-space images of the second harmonic from various metasurfaces. The top row contains the poled metasurfaces and shows an exemplary scheme of $\chi^{(2)}$-distributions, and the bottom row contains the nonpoled metasurfaces. (a) Poled 1D metasurface (nanograting) with structure period $d = 1.2$ μm and ridge width 0.6 μm, poling period $p = 2$ μm, excited with the nonresonant pump wavelength ~1550 nm. (e) Corresponding nonpoled 1D metasurface (nanograting) with the same $d$ and ridge width. (b) and (c) poled 2D metasurfaces with structure period $d = 1$ μm, poling period $p = 2$ μm, excited with the nonresonant pump wavelength 1412 nm. In (b), the nanoresonators are supposed to be either completely poled ($-\chi^{(2)}$) or completely nonpoled ($\chi^{(2)}$). In (c), the domain border is supposed to be inside a nanoresonator based on the relative positioning of the fabricated nanoresonator array with respect to the poled regions of the thin film. (d) Poled 2D metasurface with the same geometric parameters as in (b) and (c), but the poling period is $p = 3$ μm. (f)–(h) Nonpoled metasurfaces with the same $d = 1$ μm and geometry of the nanoresonators. Each image is normalized to its maximum SHG value, and the pump polarization is oriented along the LN optic axis, which is shown as a white arrow. (i) Integrated SHG signal from metasurfaces in (a)–(h). The values extracted from (a) and (e) are multiplied by 10. SHG is normalized to the value from (d), and the error bars account for a pump power variation of 10%.

the substrate, we can clearly observe an enhanced signal at the positions of nanoresonators in Figs. 2(a)–2(h) and even identify single resonators. Interestingly, one can easily notice a difference between the second-harmonic distributions of poled metasurfaces and their nonpoled twins: poled metasurfaces show an additional modulation in the spatial distribution of the SH, from which we can estimate the poling period to be roughly matching the design value. The most prominent example is Fig. 2(d) with a poling period $p = 3$ μm, where we observe three brighter nanoresonator rows in a distance of ~3 μm.

The 1D metasurfaces in Figs. 2(a) and 2(e) have a structure period of $d = 1.2$ μm and a ridge width of 0.6 μm. They were excited with a nonresonant pump wavelength of ~1550 nm. In both Figs. 2(a) and 2(b), we can observe bright horizontal stripes, which are the LN ridges. The 2D metasurfaces in Figs. 2(b)–2(d) and 2(f)–2(h) have the same (designed) geometric parameters: nanoresonators were designed as cuboids with side lengths of 0.69 μm and periods $d = 1$ μm (but fabricated as truncated pyramids). The only difference is the poling period and the position of the domain border: for Fig. 2(b) $p = 2$ μm, each nanoresonator column is either poled or nonpoled, meaning an alternating $\chi^{(2)}$-sign in the neighboring columns; for Fig. 2(c) $p = 2$ μm, the domain border nominally is inside the nanoresonators, meaning every nanoresonator has one half with $\chi^{(2)}$ and another with $-\chi^{(2)}$; and for Fig. 2(d) $p = 3$ μm some domain borders also are inside the nanoresonators. Comparing Figs. 2(b) and 2(c), we observe that the additional periodicity is less noticeable for Fig. 2(c)

than for Fig. 2 (b), which is likely due to the domain border inside the nanoresonators in Fig. 2(c). The bar plot in Fig. 2(i) summarizes the experimental SHG efficiencies for Figs. 2(a)–2(h), where the error bars account for a pump power variation of 10%. It is evident that 1D metasurfaces emit 20 times less SH compared to 2D metasurfaces despite the larger filling factor. For a 1D metasurface, the nonlinear material LN makes 50% of one unit cell volume in contrast to 40% for a 2D metasurface. However, the 1D metasurfaces have lower electric field enhancements, and the variation of LN substrate thickness below can lead to different collected SHG. According to our simulations, the SH signal from a poled metasurface should be approximately the same as from a nonpoled metasurface when pumped not in a resonance [simulations are done for Fig. 2(b) and Fig. 2(f) metasurfaces], which is confirmed by our experiments. The difference in the SHG between pairs of metasurfaces is likely due to the poling inhomogeneity and different LN substrate thicknesses.

Before moving to the SHG diffraction patterns, let us discuss the way they are plotted. Unfortunately, our EMCCD camera shows a strong blooming effect: vertical lines going through pixels with a strong signal, originating from the spread of the electric charge into other pixels on the same vertical, as shown in Figs. 3(c)–(f). To remove the blooming signature from the plots, for every image we select a rectangular region on the top containing the blooming part but no SHG, take a mean value of each column, and subtract this line from the rest of the image. Subsequently, all negative pixels are set to 0.01.
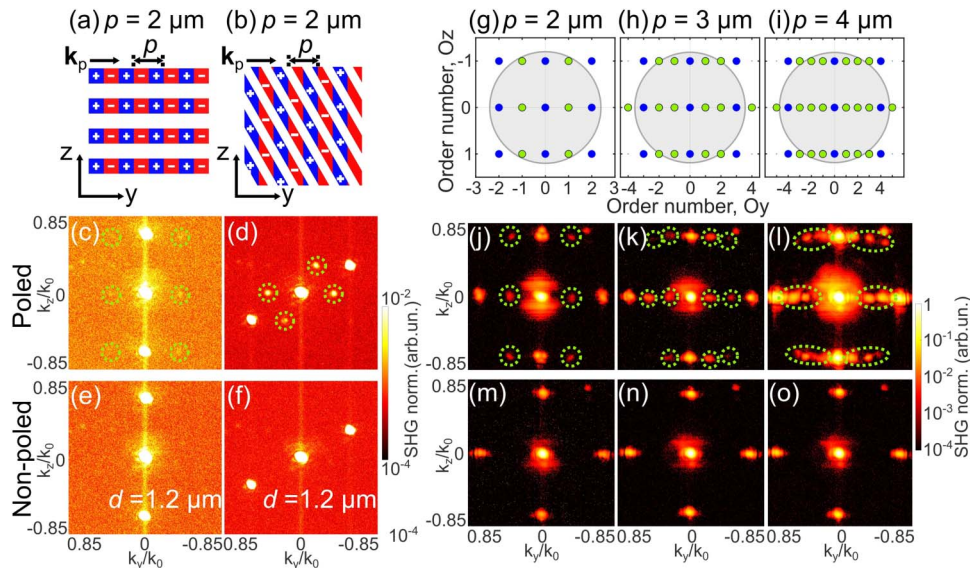


**Fig. 3.** (a), (b) Sketches of 1D poled metasurfaces and (c)–(f) experimental images of SH diffraction patterns of 1D poled metasurfaces with LN ridges (c) along *y*-axis and (d) rotated by 60°, as well as nonpoled reference metasurfaces, (e) and (f), correspondingly. The poling period is $p = 2$ μm, the nanograting period is $d = 1.2$ μm, and the ridge width is 0.6 μm. The pump wavelength is ~1550 nm, and the polarization is along the LN optic axis. The vertical lines coming through the 0th and 1st geometric orders are associated with the blooming effect of the EMCCD camera. The SHG in each image (c)–(f) is normalized to its maximum value. $\mathbf{k}_p$ marks the nonlinear grating wavevector. (g)–(i) Analytical and (j)–(l) experimental images of SH diffraction patterns of 2D poled metasurfaces with poling periods (g) and (j) $p = 2$ μm, (h) and (k) 3 μm, and (i) and (l) 4 μm. (m)–(o) Corresponding nonpoled metasurfaces. The blue dots mark the geometric diffraction orders, and the green dots mark nonlinear $\chi^{(2)}$-orders. The gray circles in (g)–(i) correspond to the NA of our collecting objective. The pump wavelength is 1412 nm, and polarization is along the LN optic axis. SHG in each image (j)–(o) is normalized to its maximum value and plotted on a logarithmic scale. The green circles in all subfigures mark the diffraction orders associated with the $\chi^{(2)}$-grating.

This is done to improve the contrast between the diffraction orders and the surrounding area. In each image, the SHG is then normalized to the exposure time and incident average power squared. As the last step, we normalize the SHG to the maximum value in each image and then plot the result on a logarithmic scale to see both strong geometric diffraction orders and rather weak $\chi^{(2)}$-orders.

Next, we study the SHG diffraction pattern. The variation of the nonlinear susceptibility $\chi^{(2)}$ acts as a nonlinear grating with the wavevector perpendicular to the LN optic axis $\mathbf{k}_p$ [see, for example, Figs. 3(a) and 3(b)]. Thus, it results in additional SH diffraction orders along $\mathbf{k}_y$. In all metasurfaces studied in this work, the 0th and the 1st geometric orders appear much stronger than the orders from the $\chi^{(2)}$-grating. This is due to the fact that these geometric orders also contain SH generated in the LN substrate, which subsequently diffracts. Furthermore, because of the metasurface's small width of 20 μm, we additionally observe diffraction from the edges of the metasurface. This leads to the broadening of the 0th order with a strong signal on top and bottom.

Figure 3 shows SH diffraction patterns for different metasurfaces for nonresonant pump wavelengths (~1550 nm for 1D metasurfaces, 1412 nm for 2D metasurfaces). For the poled 1D metasurface in Fig. 3(c), which is the same metasurface as in Fig. 2(a), we observe nine diffraction orders; however, its nonpoled twin in Fig. 3(e) shows only three diffraction orders. Thus, we can deduce that the three orders in Fig. 3(c), visible for the nonpoled metasurface, are generated by the nanograting geometry while the six additional ones (marked with green circles) are due to the $\chi^{(2)}$-grating. We explore controlling the SHG diffraction by rotating the nanograting by 60° with respect to the $\chi^{(2)}$-grating, as shown in Fig. 3(b). This configuration generates seven orders; the nonpoled metasurface in Fig. 3(f) still shows only three orders. Note that for Figs. 3(c)–3(f) we did not subtract the noise since the SHG in the $\chi^{(2)}$ diffraction orders is weaker than the EMCCD blooming, which is observable as vertical lines.

To estimate the amount of diffraction orders for different periods, we find all propagating diffraction orders for the SH by solving the grating equation for the SH wavelength 706 nm. The results are shown on the top of Figs. 3(g)–3(i): The blue dots mark the geometric diffraction orders while the green dots signify orders created by the modulated nonlinearity $\chi^{(2)}$. The gray circle indicates the numerical aperture (NA) of our collection optics. In the experiment, the orders outside this circle were cut by the NA of our collecting objective. This analytical prediction is in very good agreement with the experimental results from poled 2D metasurfaces in Figs. 3(j)–3(l), where additional orders appear compared to the nonpoled arrays in Figs. 3(m)–3(o). To verify their origin, we plot SHG diffraction patterns for metasurfaces with the same nanostructures' period $d$ but different poling periods $p$: Fig. 3(j), 2 μm; Fig. 3(k), 3 μm; and Fig. 3(l), 4 μm. As expected, we observe that increasing $p$ increases the amount of orders that are captured within our finite collection NA. For $p = 2$ μm, we measure six nonlinear diffraction orders, marked with green, which coincide with the doubled periodicity in the $y$-direction. When going to $p = 3$ μm, 12 additional orders appear, the outer ones on top and bottom are cut. For $p = 4$ μm, the reduced distance in the $k$-space between the nonlinear orders makes it more difficult to distinguish them. The very good agreement between these observed diffraction patterns and our theoretical prediction confirms the capability of electric field poling to tailor SHG from metasurfaces.

Another typical feature of nanostructured metasurfaces is localized resonances. Thus, the next question we address is how Mie-type resonances influence SHG in metasurfaces with structured $\chi^{(2)}$. For this issue, we pump the metasurface pairs from Figs. 3(j)–3(o) at different wavelengths to compare three cases: nonresonant excitation, pump at the ED resonance, and pump at the MD resonance. Figure 4 shows the results for the pair with poling period $p = 2$ μm [the same metasurfaces as in Figs. 2(b), 2(f), 3(j), and 3(m)] and the three wavelengths: 1412 nm with no resonance, 1445 nm with ED resonance,
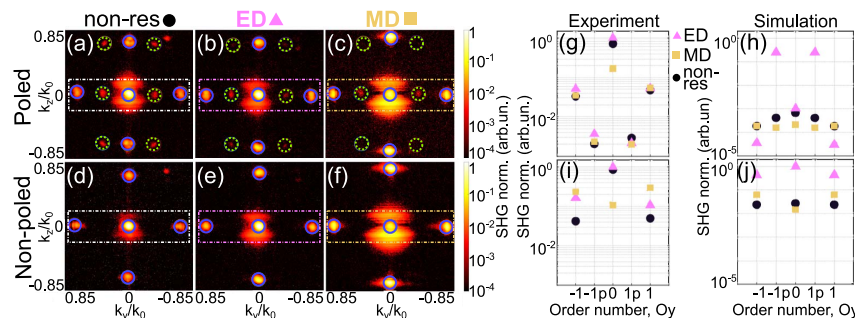


**Fig. 4.** (a)–(f) Experimental images of the SH diffraction pattern from poled (top row) with poling period $p = 2$ μm and nonpoled (bottom row) metasurfaces for different pump wavelengths: (a) and (d) pump 1412 nm, nonresonant case, (b) and (e) pump 1456 nm, electric dipole resonance, (c) and (f) pump 1565 nm, magnetic dipole resonance. Polarization is along the optic axis. Geometric orders are indicated by blue circles, and nonlinear orders are indicated by green circles. Dash-dotted rectangles mark the orders used in (g) and (i). SHG is normalized to the maximum value in each plot. (g) Experimental and (h) simulated SHG signals for the orders from the central row $(n, 0)$, where $n = \{\pm 1, \pm 1p, 0\}$ for poled metasurfaces in (a)–(c). Similarly, (i) experimental and (j) simulated SHG signals for the orders from the central row for nonpoled metasurfaces in (d)–(f). Geometric orders are indicated as 0 and $\pm 1$, and nonlinear orders are indicated as $\pm 1p$. The SHG signal in each order was calculated by integration inside corresponding blue (linear) or green (nonlinear) circles. In (g) and (i) SHG values are normalized to the value of $(0,0)$ for ED for each respective case. The LN substrate thickness in the simulations is 750 nm.

and 1565 nm with MD resonance. Because of the fabrication tolerances, for this metasurface note that the ED resonance appears at a slightly shifted wavelength compared to the metasurface in Fig. 1(d).

For all the three pump wavelengths, $\chi^{(2)}$-orders are visible, and they become weaker as the wavelength increases, as shown by the decreasing signal in the green circles in Figs. 3 and 4. To compare their intensities, we integrate the SHG signal for the diffraction orders for $k_z = 0$ and plot them in Figs. 4(g) and 4(i). In the following, we will label the $k_z = 0$ orders as $(n, 0)$, where $n = \{\pm 1, \pm 1p, 0\}$, geometric orders are indicated as $(0, 0)$ and $(\pm 1, 0)$, and $\chi^{(2)}$-orders as $(\pm 1p, 0)$. Although the 0th order is larger, we still integrate within a circle that is with the same size as the others.

To better understand the effects at play, we perform numerical simulations with COMSOL Multiphysics software. We demonstrate the main effects of poling using one set of geometric parameters of the 2D metasurface depicted in Figs. 2(b), 2(f), 4(j), and 4(m): structure period $d = 0.98$ μm, poling period $p = 2$ μm, top length of the truncated pyramid 520 nm, bottom length 880 nm, and thickness 590 nm. The pyramid is placed on 2 μm SiO$_2$ on a thick LN substrate. The geometry of the nanoresonators used in simulations was adjusted to match the experimental spectra. Since we illuminate ~9 × 9 nanoresonators in the experiment and the pump wavelengths are sufficiently far from the lattice resonance (in this work it is 1 μm for the air interface) simulating an infinite

metasurface is a justified approximation [32,33]. However, we do not account for the triangular domain shape of the periodic poling in the simulations, as shown in Fig. 1(c), and instead assume it to be rectangular. With this, we model the poled metasurface with a unit cell containing two nanoresonators, where $\chi^{(2)}$ has equal magnitude but opposite signs in both resonators. The nonpoled metasurface is implemented with one resonator per unit cell and the usual sign of $\chi^{(2)}$. The simulations follow the two-step approach described in Refs. [1,10]. First, in the linear simulation, we use plane wave excitation to calculate the electromagnetic field at the pump wavelength, which is then taken to compute the nonlinear polarization inside the nanoresonators. In a second simulation step, this nonlinear polarization serves as a source for the emitted light of the SH. We used the following values for the nonlinear susceptibility tensor $d_{22} = 1.9$ pm/V, $d_{31} = -3.2$ pm/V, and $d_{33} = -19.5$ pm/V [36].

At the ED resonance, the electric field inside the nanoresonators is predominantly oriented along the z-axis, as shown in Fig. 1(f). Thus, at the ED resonance, we use the largest element of second-order nonlinear susceptibility $d_{33}$ [37] combined with the highest electric field enhancement, as shown in Fig. 1(f). Therefore, we expect the $\chi^{(2)}$-orders at this wavelength to show a stronger SHG signal than at other wavelengths. In our nonlinear simulations, the overall SHG and in particular the SHG in the nonlinear orders at the ED resonance are stronger than at other wavelengths, as shown in Fig. 4(h). For the nonpoled metasurface in Fig. 4(j), the simulated SHG
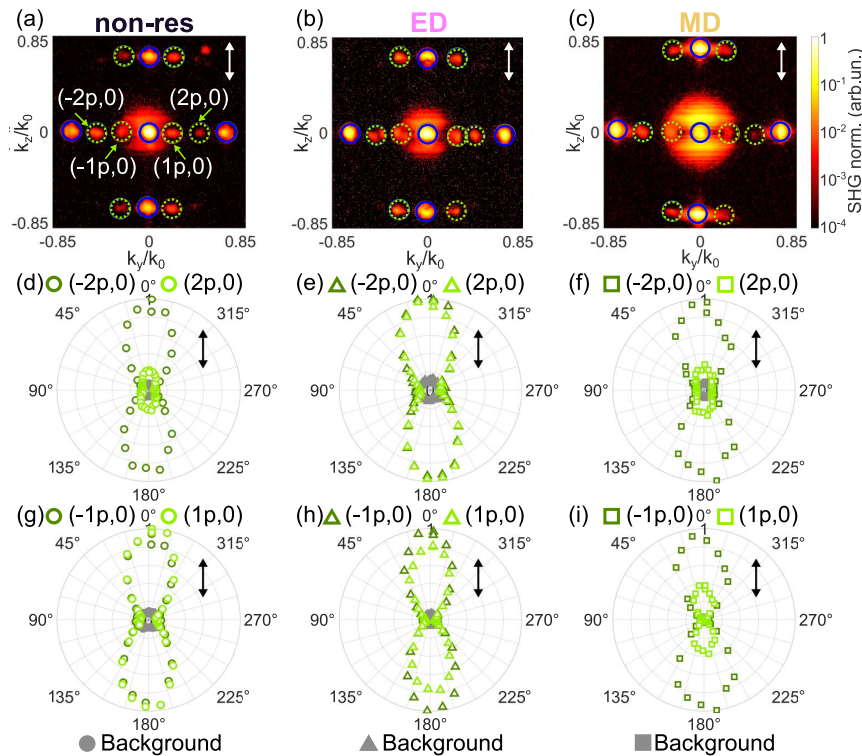


**Fig. 5.** (a)–(c) SHG diffraction patterns for the metasurface with poling period $p = 3$ μm for the pump wavelengths: (a) nonresonant, at the (b) ED resonance and (c) MD resonance. The orders (0,0), ($\pm 1$, 0), and (0, $\pm 1$) are the geometric orders and are marked blue. The orders ($\pm 1p$, 0), ($\pm 2p$, 0), and (0, $\pm 1p$) are $\chi^{(2)}$-orders and are marked green. The white and black arrows show the polarization direction along the LN optic axis. The SHG is normalized to the maximum value. (d)–(f) The SHG for different pump polarizations in ($\pm 2p$, 0) and (g)–(i) in ($\pm 1p$, 0) orders. The values are normalized to the maximum value in each plot. Gray circles/triangles/squares show the background.

is also stronger at the wavelength of the ED resonance. Note, however, that in our simulations we can only include a finite thickness of the LN substrate and therefore cannot fully account for the effect of the background SHG from the LN substrate. For this reason, the geometric orders $(\pm 1, 0)$, into which the substrate SHG is emitted, are expected to be more pronounced in the experiment than in the simulation.

When we compare poled and nonpoled metasurfaces, the excited modes are the same at the fundamental wavelength, but they can differ at the SH wavelength. Because our metasurfaces possess Mie-type modes strongly coupled to the lattice periodicity [31], the $\chi^{(2)}$-grating naturally changes the "effective" lattice for the SH. With poling, we gain an additional tool to control the mode at the SH frequency.

Another interesting question is how the SHG intensity varies when changing the pump polarization. Since for the 0th and 1st diffraction orders, SHG from both the substrate and metasurface contributes, we concentrate on the $\chi^{(2)}$-orders. In Figs. 5(a)–5(c), we demonstrate the SHG diffraction patterns for the metasurface with a $p = 3$ μm poling period for nonresonant and two resonant cases, ED and MD. Also in Figs. 5(d)–5(i), we plot how the SHG signal depends on pump polarization for four $\chi^{(2)}$-orders at $k_z = 0$, $(\pm 2p, 0)$, and $(\pm 1p, 0)$. For all wavelengths, it is an eight-like shape where the most signal is emitted when the excitation is polarized along the LN optic axis [1,38], where we use the strongest element of nonlinear tensor $d_{33}$. Although we previously showed that other elements of the second-order nonlinear coefficient [1] also generate measurable SH for 90° and 270° excitation when pumping at the MD resonance, here it is not the case because these metasurfaces have a different mode composition and field enhancement.

## 3. CONCLUSION

After demonstrating the effect of adding a nonlinear $\chi^{(2)}$-grating on the emitted SH, we want to discuss the routes to improve this method to control SHG. We note that poling often produces triangular domains, which of course would influence the SHG. In our case, the domains also may not always extend over the full thin film width. Increasing the poling homogeneity laterally (achieving a full domain inversion of desired shape; e.g., a stripe) and in-depth (achieving full domain inversion along the whole thickness of the LN thin film) should improve the diffraction efficiency into the $\chi^{(2)}$-orders.

Using aperiodic poling and pattern poling, we can shape the SHG diffraction and enrich the $k$-space. Alternatively to electric field poling one can use, for example, femtosecond IR [39,40] or UV [41] pulses to make use of the pyroelectric property of LN. With this, domains as small as 100 nm were achieved on $z$-cut LN [42].

Inspired by thick LN crystals, poling can be used to produce vortex beams [43,44] or Hermite–Gaussian and Laguerre–Gaussian beams [45]. Because the SHG phase generated from $-\chi^{(2)}$ and $\chi^{(2)}$ domains has a phase shift, it is possible to harvest it into SHG modulation and create nonlinear holograms. Our approach can also be extended for metasurfaces from different

materials (GaN [41], 2D materials), which opens new possibilities for SHG control.

In conclusion, we successfully fabricated resonant metasurfaces from periodically poled $x$-cut LN thin films. We demonstrated that by changing the poling period we can engineer the spatial distribution of the nonlinearity and tailor the SHG diffraction pattern. Thus, metasurfaces from poled LN offer new degrees of freedom to control SHG in resonant metasurfaces.

**Disclosures.** The authors declare no conflicts of interest.

**Data Availability.** Data underlying the results presented in this paper are not publicly available at this time but may be obtained from the authors upon reasonable request.

## REFERENCES

1. A. Fedotova, M. Younesi, J. Sautter, A. Vaskin, F. J. Löchner, M. Steinert, R. Geiss, T. Pertsch, I. Staude, and F. Setzpfandt, "Second-harmonic generation in resonant nonlinear metasurfaces based on lithium niobate," Nano Lett. **20**, 8608–8614 (2020).
2. P. P. Vabishchevich, S. Liu, M. B. Sinclair, G. A. Keeler, G. M. Peake, and I. Brener, "Enhanced second-harmonic generation using broken symmetry III–V semiconductor Fano metasurfaces," ACS Photon. **5**, 1685–1690 (2018).
3. V. F. Gili, L. Carletti, A. Locatelli, D. Rocco, M. Finazzi, L. Ghirardini, I. Favero, C. Gomez, A. Lemaître, M. Celebrano, and C. De Angelis, "Monolithic AlGaAs second-harmonic nanoantennas," Opt. Express **24**, 15965–15971 (2016).
4. F. J. Löchner, R. Mupparapu, M. Steinert, A. George, Z. Tang, A. Turchanin, T. Pertsch, I. Staude, and F. Setzpfandt, "Controlling second-harmonic diffraction by nano-patterning $MoS_2$ monolayers," Opt. Express **27**, 35475–35484 (2019).
5. D. Rocco, A. Zilli, A. Ferraro, A. Borne, V. Vinel, G. Leo, A. Lemaître, C. Zucchetti, M. Celebrano, R. Caputo, and C. De Angelis, "Tunable second harmonic generation by an all-dielectric diffractive metasurface embedded in liquid crystals," New J. Phys. **24**, 045002 (2022).
6. G. Marino, D. Rocco, C. Gigli, G. Beaudoin, K. Pantzas, S. Suffit, P. Filloux, I. Sagnes, G. Leo, and C. De Angelis, "Harmonic generation with multi-layer dielectric metasurfaces," Nanophotonics **10**, 1837–1843 (2021).
7. R. Sarma, J. Xu, D. de Ceglia, L. Carletti, J. Klem, M. A. Belkin, and I. Brener, "Control of second-harmonic generation in all-dielectric intersubband metasurfaces by controlling the polarity of $\chi^{(2)}$," Opt Express **30**, 34533–34544 (2022).
8. L. Carletti, A. Zilli, F. Moia, A. Toma, M. Finazzi, C. De Angelis, D. N. Neshev, and M. Celebrano, "Steering and encoding the polarization of the second harmonic in the visible with a monolithic $LiNbO_3$ metasurface," ACS Photon. **8**, 731–737 (2021).

9. J. Ma, F. Xie, W. Chen, J. Chen, W. Wu, W. Liu, Y. Chen, W. Cai, M. Ren, and J. Xu, "Nonlinear lithium niobate metasurfaces for second harmonic generation," Laser Photon. Rev. **15**, 2000521 (2021).

10. T. Santiago-Cruz, A. Fedotova, V. Sultanov, M. A. Weissflog, D. Arslan, M. Younesi, T. Pertsch, I. Staude, F. Setzpfandt, and M. Chekhova, "Photon pairs from resonant metasurfaces," Nano Lett. **21**, 4423–4429 (2021).

11. J. Zhang, J. Ma, M. Parry, M. Cai, R. Camacho-Morales, L. Xu, D. N. Neshev, and A. A. Sukhorukov, "Spatially entangled photon pairs from lithium niobate nonlocal metasurfaces," Sci. Adv. **8**, eabq4240 (2022).

12. V. Y. Shur, A. Akhmatkhanov, and I. Baturin, "Micro-and nano-domain engineering in lithium niobate," Appl. Phys. Rev. **2**, 040604 (2015).

13. G. Schreiber, D. Hofmann, W. Grundkoetter, Y. L. Lee, H. Suche, V. Quiring, R. Ricken, and W. Sohler, "Nonlinear integrated optical frequency converters with periodically poled Ti:LiNbO₃ waveguides," Proc. SPIE **4277**, 144–160 (2001).

14. C. Wang, C. Langrock, A. Marandi, M. Jankowski, M. Zhang, B. Desiatov, M. M. Fejer, and M. Lončar, "Ultrahigh-efficiency wavelength conversion in nanophotonic periodically poled lithium niobate waveguides," Optica **5**, 1438–1441 (2018).

15. J. Lin, F. Bo, Y. Cheng, and J. Xu, "Advances in on-chip photonic devices based on lithium niobate on insulator," Photon. Res. **8**, 1910–1936 (2020).

16. P. Mutter, K. M. Mølster, A. Zukauskas, V. Pasiskevicius, and C. Canalias, "Highly-efficient first-order backward second-harmonic generation in periodically poled Rb-doped KTP with a period of 317 nm," in *Optica Advanced Photonics Congress* (Optica Publishing Group, 2022), paper NpTu1G.1.

17. M. Conforti, C. De Angelis, U. K. Sapaev, and G. Assanto, "Pulse shaping via backward second harmonic generation," Opt. Express **16**, 2115–2121 (2008).

18. M. Lauritano, A. Parini, G. Bellanca, S. Trillo, M. Conforti, A. Locatelli, and C. De Angelis, "Bistability, limiting, and self-pulsing in backward second-harmonic generation: a time-domain approach," J. Opt. A **8**, S494 (2006).

19. C. Canalias and V. Pasiskevicius, "Mirrorless optical parametric oscillator," Nat. Photonics **1**, 459–462 (2007).

20. A. C. Nutt, V. Gopalan, and M. C. Gupta, "Domain inversion in LiNbO₃ using direct electron-beam writing," Appl. Phys. Lett. **60**, 2828–2830 (1992).

21. D. Wei, C. Wang, H. Wang, X. Hu, D. Wei, X. Fang, Y. Zhang, D. Wu, Y. Hu, J. Li, and S. Zhu, "Experimental demonstration of a three-dimensional lithium niobate nonlinear photonic crystal," Nat. Photonics **12**, 596–600 (2018).

22. G. Rosenman, P. Urenski, A. Agronin, Y. Rosenwaks, and M. Molotskii, "Submicron ferroelectric domain structures tailored by high-voltage scanning probe microscopy," Appl. Phys. Lett. **82**, 103–105 (2003).

23. V. Berger, "Nonlinear photonic crystals," Phys. Rev. Lett. **81**, 4136–4139 (1998).

24. A. Arie and N. Voloch, "Periodic, quasi-periodic, and random quadratic nonlinear photonic crystals," Laser Photon. Rev. **4**, 355–373 (2010).

25. N. Broderick, G. Ross, H. Offerhaus, D. Richardson, and D. Hanna, "Hexagonally poled lithium niobate: a two-dimensional nonlinear photonic crystal," Phys. Rev. Lett. **84**, 4345–4348 (2000).

26. J. Zhao, M. Rüsing, M. Roeper, L. M. Eng, and S. Mookherjea, "Poling thin-film *x*-cut lithium niobate for quasi-phase matching with submicrometer periodicity," J. Appl. Phys. **127**, 193104 (2020).

27. J. T. Nagy and R. M. Reano, "Submicrometer periodic poling of lithium niobate thin films with bipolar preconditioning pulses," Opt. Mater. Express **10**, 1911–1920 (2020).

28. M. Younesi, R. Geiss, S. Rajaee, F. Setzpfandt, Y.-H. Chen, and T. Pertsch, "Periodic poling with a micrometer-range period in thin-film lithium niobate on insulator," J. Opt. Soc. Am. B **38**, 685–691 (2021).

29. B. Slautin, H. Zhu, and V. Y. Shur, "Submicron periodical poling in *z*-cut lithium niobate thin films," Ferroelectrics **576**, 119–128 (2021).

30. Y. Dong and Q. Dong, "Precise control of nanodomain size in LiNbO₃," Mater. Res. Express **5**, 035004 (2018).

31. V. E. Babicheva and A. B. Evlyukhin, "Multipole lattice effects in high refractive index metasurfaces," J. Appl. Phys. **129**, 040902 (2021).

32. V. Zakomirnyi, A. Ershov, V. Gerasimov, S. Karpov, H. Ågren, and I. Rasskazov, "Collective lattice resonances in arrays of dielectric nanoparticles: a matter of size," Opt. Lett. **44**, 5743–5746 (2019).

33. L. Ciarella, A. Tognazzi, F. Mangini, C. De Angelis, L. Pattelli, and F. Frezza, "Finite-size and illumination conditions effects in all-dielectric metasurfaces," Electronics **11**, 1017 (2022).

34. Y. Yang, I. I. Kravchenko, D. P. Briggs, and J. Valentine, "All-dielectric metasurface analogue of electromagnetically induced transparency," Nat. Commun. **5**, 5753 (2014).

35. S. Campione, S. Liu, L. I. Basilio, L. K. Warne, W. L. Langston, T. S. Luk, J. R. Wendt, J. L. Reno, G. A. Keeler, I. Brener, and M. B. Sinclair, "Broken symmetry dielectric resonators for high quality factor Fano metasurfaces," ACS Photon. **3**, 2362–2367 (2016).

36. I. Shoji, T. Kondo, A. Kitamoto, M. Shirane, and R. Ito, "Absolute scale of second-order nonlinear-optical coefficients," J. Opt. Soc. Am. B **14**, 2268–2294 (1997).

37. R. W. Boyd, *Nonlinear Optics* (Academic, 2019).

38. F. Timpu, J. Sendra, C. Renaut, L. Lang, M. Timofeeva, M. T. Buscaglia, V. Buscaglia, and R. Grange, "Lithium niobate nanocubes as linear and nonlinear ultraviolet Mie resonators," ACS Photon. **6**, 545–552 (2019).

39. X. Chen, P. Karpinski, V. Shvedov, K. Koynov, B. Wang, J. Trull, C. Cojocaru, W. Krolikowski, and Y. Sheng, "Ferroelectric domain engineering by focused infrared femtosecond pulses," Appl. Phys. Lett. **107**, 141102 (2015).

40. X. Xu, T. Wang, P. Chen, C. Zhou, J. Ma, D. Wei, H. Wang, B. Niu, X. Fang, D. Wu, S. Zhu, M. Gu, M. Xiao, and Y. Zhang, "Femtosecond laser writing of lithium niobate ferroelectric nanodomains," Nature **609**, 496–501 (2022).

41. A. Chowdhury, H. M. Ng, M. Bhardwaj, and N. G. Weimann, "Second-harmonic generation in periodically poled GaN," Appl. Phys. Lett. **83**, 1077–1079 (2003).

42. A. Boes, V. Sivan, G. Ren, D. Yudistira, S. Mailis, E. Soergel, and A. Mitchell, "Precise, reproducible nano-domain engineering in lithium niobate crystals," Appl. Phys. Lett. **107**, 022901 (2015).

43. N. V. Bloch, K. Shemer, A. Shapira, R. Shiloh, I. Juwiler, and A. Arie, "Twisting light by nonlinear photonic crystals," Phys. Rev. Lett. **108**, 233902 (2012).

44. D. Wei, C. Wang, X. Xu, H. Wang, Y. Hu, P. Chen, J. Li, Y. Zhu, C. Xin, X. Hu, and Y. Zhang, "Efficient nonlinear beam shaping in three-dimensional lithium niobate nonlinear photonic crystals," Nat. Commun. **10**, 4193 (2019).

45. A. Shapira, R. Shiloh, I. Juwiler, and A. Arie, "Two-dimensional nonlinear beam shaping," Opt. Lett. **37**, 2136–2138 (2012).